A Modified Critical State Two-surface Plasticity Model for Sand

Theory and Implementation

Bakmar, Christian LeBlanc; Hededal, O.; Ibsen, Lars Bo

Publication date:
2008

Document Version
Publisher's PDF, also known as Version of record

A modified critical state two-surface plasticity model for sand - theory and implementation

C. LeBlanc
O. Hededal
L. B. Ibsen

ISSN 1901-7278
DCE Technical Memorandum No. 8

AALBORG UNIVERSITY
Department of Civil Engineering

Aalborg University
Department of Civil Engineering
Water & Soil

DCE Technical Memorandum No. 8

A modified critical state two-surface plasticity model for sand - theory and implementation

by

C. LeBlanc
O. Hededal
L. B. Ibsen

December 2008

Scientific Publications at the Department of Civil Engineering

Technical Reports are published for timely dissemination of research results and scientific work carried out at the Department of Civil Engineering (DCE) at Aalborg University. This medium allows publication of more detailed explanations and results than typically allowed in scientific journals.

Technical Memoranda are produced to enable the preliminary dissemination of scientific work by the personnel of the DCE where such release is deemed to be appropriate. Documents of this kind may be incomplete or temporary versions of papers—or part of continuing work. This should be kept in mind when references are given to publications of this kind.

Contract Reports are produced to report scientific work carried out under contract. Publications of this kind contain confidential matter and are reserved for the sponsors and the DCE. Therefore, Contract Reports are generally not available for public circulation.

Lecture Notes contain material produced by the lecturers at the DCE for educational purposes. This may be scientific notes, lecture books, example problems or manuals for laboratory work, or computer programs developed at the DCE.

Theses are monograms or collections of papers published to report the scientific work carried out at the DCE to obtain a degree as either PhD or Doctor of Technology. The thesis is publicly available after the defence of the degree.

Latest News is published to enable rapid communication of information about scientific work carried out at the DCE. This includes the status of research projects, developments in the laboratories, information about collaborative work and recent research results.

Published 2008 by
Aalborg University
Department of Civil Engineering
Sohngaardsholmsvej 57,
DK-9000 Aalborg, Denmark

Printed in Aalborg at Aalborg University

ISSN 1901-7278
DCE Technical Memorandum No. 8

Recent publications in the DCE Technical Memorandum Series

Material-point method analysis of bending in elastic beams. / Andersen, Søren Mikkel ; Andersen, Lars. Aalborg : Department of Civil Engineering : Aalborg University, 2007. 28 s. (DCE Technical Memorandum; 7).

Lumped-parameter models for windturbine footings on layered ground. / Andersen, Lars. Aalborg : Department of Civil Engineering : Aalborg University, 2007. 28 s. (DCE Technical Memorandum; 6).

Do Lumped-Parameter Models Provide the Correct Geometrical Damping? / Andersen, Lars. Aalborg : Department of Civil Engineering : Aalborg University, 2007. 32 s. (DCE Technical Memorandum; 5).

Kravmodel for det Det Digitale Byggeri : DACaPo kommentar. / Christiansson, Per. Aalborg : Aalborg University : Department of Civil Engineering, 2006. 14 s. (DCE Technical Memorandum; 4).

Kommentar til informationsniveauer og modeltyper : B3D og 3D arbejdsmetoder : Det Digitale Byggeri. / Christiansson, Per ; Svidt, Kjeld. Aalborg : Aalborg University : Department of Civil Engineering, 2006. 8 s. (DCE Technical Memorandum; 3).

Høringskommentarer vedr. 3D CAD manual 2007 : overordnede kommentarer vedrørende Del 1 : 3D arbejdsmetode og Del 2 : Metodeanvisning. / Christiansson, Per ; Svidt, Kjeld. Aalborg : Aalborg University : Department of Civil Engineering, 2006. 6 s. (DCE Technical Memorandum; 2).

Assessment of Time Functions for Piles Driven in Clay. / Augustesen, Anders ; Andersen, Lars ; Sørensen, Carsten Steen. Aalborg : Department of Civil Engineering : Aalborg University, 2006. 22 s. (DCE Technical Memorandum; 1).

ISSN 1901-7278
DCE Technical Memorandum No. 8

A modified critical state two-surface plasticity model for sand - theory and implementation

C. LeBlanc[1,2,*] O. Hededal[3] and L. B. Ibsen[1]

[1] *Department of Civil Engineering, Aalborg University, 9000 Aalborg, Denmark*
[2] *Department of Offshore Technology, DONG Energy, 2450 Copenhagen SV, Denmark*
[3] *Department of Civil Engineering, Technical University of Denmark, 2800 Kgs. Lyngby, Danmark*

SUMMARY

This paper provides background information and documentation for the implementation of a robust plasticity model as a user-subroutine in the commercial finite difference code, FLAC3D by Itasca. The plasticity model presented is equal to the 3 dimensional critical state two-surface plasticity model for sands by Manzari *et al.*, but uses a modified multi-axial surface formulation based on a versatile shape function prescribing a family of smooth and convex contours in the π-plane. The model is formulated within the framework of critical state soil mechanics and is capable of accurately simulating volumetric and stress-strain behaviour under monotonic and cyclic loading and thereby related observations like accumulation of pore pressure, cyclic mobility and cyclic liquefaction. The plasticity model is implemented with an integration scheme based on the general return mapping algorithm. The integration scheme faces convergence difficulties, primarily at very low mean effective stresses. The convergence problems are addressed by suitable correction strategies designed to add robustness, stability and efficiency to the integration scheme. An outline of all model parameters is given with suggestions for parameter reductions.

KEY WORDS: constitutive modeling; granular materials; critical state; bounding surface; return mapping method; implementation strategy

1. INTRODUCTION

Over the last decades, plasticity models that accurately simulate stress-strain behaviour of materials have been successfully used within several engineering disciplines. However, for granular materials, only simple classical elasto-plastic models are supported by most commercial engineering codes, e.g. Mohr-Coulomb and Cam-Clay. While these models are useful for many geotechnical problems, they are insufficient for more complex problems. More advanced models may be required to accurately simulate the response of soil under a wide range of relative densities and mean effective stress levels. Also, advanced models are required to simulate the response to cyclic loading and related observations such as accumulation of

*Correspondence to: C. LeBlanc, Dept. of Offshore Technology, DONG Energy, A.C.Meyers Vænge 9, 2450 Copenhagen SV, Denmark, E-mail: chrle@dongenergy.com

pore pressure, cyclic mobility and cyclic liquefaction. Continuum-based constitutive models simulating the cyclic behaviour of soil are primarily developed and applied within the framework of earthquake engineering in which the degradation of strength and stiffness is essential for the prediction of seismic performance of structures. The models are complex as several geotechnical features, e.g. characteristic states, critical states and failure envelopes, must be successfully simulated while accounting for a strong influence of the third stress invariant and the isotropic stress level.

The critical state soil mechanics (CSSM) [27, 28] provide a broad framework to explain the fundamental behaviour of granular materials. The success and broad recognition of the CSSM has lead to widespread application in constitutive models. The *Norsand model* [19] initially adopted the CSSM in a model formulation. Later notable critical state models include [3, 7, 13, 25, 31] and more complex models, also accounting for anisotropic stress-strain behaviour, are presented by [6, 10]. A versatile and yet simple model, formulated by within the framework of CSSM, is the *critical state two-surface plasticity model for sands* presented by Manzari et al. [23, 24]. The model has proved to successfully simulate drained and undrained stress-strain behaviour of non-cohesive sands under monotonic and cyclic loading in a wide range of confining stresses and densities [24, 30]

This paper provides background information and documentation for the implementation of a robust plasticity model as a user-subroutine in the commercial finite difference code FLAC3D (Fast Lagrangian Analysis of Continua in Three Dimensiobs) by Itasca. The constitutive model presented is equal to the two-surface critical state plasticity model for sands by Manzari et al. [23, 24], except for minor modifications. Thus, the model is denoted the *modified two-surface critical state plasticity model for sands*. The major modification is the introduction of an alternative multi-axial surface formulation based on a versatile shape function used to prescribe a family of smooth and convex contours in the π-plane. Emphasis is made to outline the physical interpretation of the plasticity model. An outline of all model parameters is given with suggestions for parameter reductions.

An efficient integration scheme based on a general return mapping algorithm originally proposed by Simo and Ortiz [29] is tailored to the plasticity model. The integration scheme is efficient, however only conditionally stable. Thus, an implementation strategy is introduced to add robustness to the integration scheme. The stability and efficiency is tested by simulations of undrained monotonic and cyclic triaxial tests. Thus, this paper provide complete information for implementation of a robust user-defined constitutive model, capable of simulating the response of non-cohesive sands, in a commercial finite difference (or finite element) code.

2. ON THE FRAMEWORK OF CRITICAL STATE SOIL MECHANICS

The concept *critical state* is successfully applied within the CSSM [27, 28]. Consider a soil sample subjected to shear loading. As shearing continues beyond peak shear stress, a state is reached after which further shearing causes zero volumetric change and zero change in shear stress, see Figure 1. This state, describing the post-peak behaviour, is referred to as the *critical state*, according to Casagrande [2]. An important outcome of the CSSM is that the critical

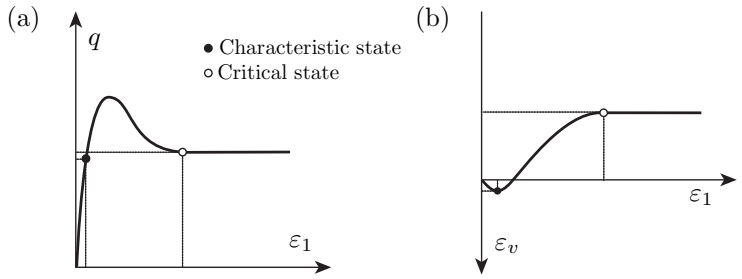

Figure 1. Outline of a typical triaxial compression test on dense sand performed under constant isotropic stress with q and ε_v converging against a constant value at critical state.

state can be represented by a straight line in p-q stress space[†], with the inclination being largely independent of both the relative density and isotropic stress level. The inclination can be defined by the *critical stress ratio*, $M_{\rm cr} = q/p$. $M_{\rm cr}$ seems to represent an intrinsic parameter and is therefore adopted as a fundamental model parameter.

At critical state, the soil particles can rearrange while the packing density remains constant. The *critical void ratio*, $e_{\rm cr}$, is used to quantify the packing density at critical state. Experiments indicate that $e_{\rm cr}$ is independent of the initial void ratio, i.e. the soil particles always self-organize toward a critical packing density when sheared beyond critical state [2]. Figure 2a schematically illustrates the void ratio converging toward $e_{\rm cr}$ under monotonic shearing. The

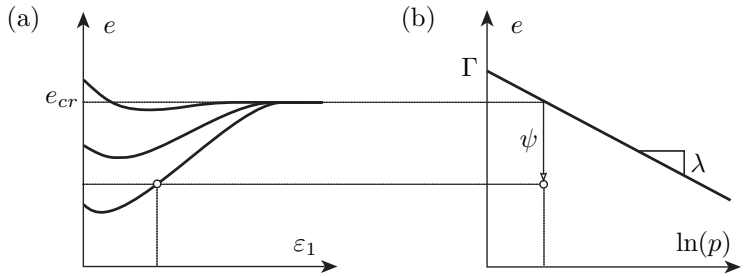

Figure 2. (a) Outline of change in void ratio obtained from triaxial compression tests of sand under a constant isotropic stress. (b) Variation of critical void ratio with isotropic stress level.

value of $e_{\rm cr}$ depends on the isotropic stress level as outlined in Figure 2b. Within the CSSM, the variation of e_{cr} and p is assumed linear in e_{cr}-ln(p) space. The line is referred to as the *critical state line*, defined by

$$e_{cr} = \Gamma - \lambda \ln\left(\frac{p}{p_{\rm u}}\right) \qquad p_{\rm u} = 1kPa \tag{1}$$

The constants λ and Γ denote the line inclination and the reference void ratio at the unit pressure $p_{\rm u}$, respectively. It is convenient to have a parameter indicating the distance to critical

[†]In this paper, all stress notations refer to effective stresses.

state. In this context, the *state parameter* is defined by

$$\psi = e - e_{cr} \tag{2}$$

with e referring to the void ratio in the current state [1]. The state parameter is an essential parameter arising from the framework of the critical state soil mechanics and has been successfully adopted for constitutive modelling. The state parameter is adopted in the current model to prescribe peak stress levels and dilatancy behaviour.

3. MODELLING THE PEAK SHEAR STRENGTH OF SANDS

It is well documented that a strong correlation exists between the relative density and the peak shear strength of sands. The typical variation of peak shear strength with isotropic pressure and relative density is outlined in Figure 3a and 3b.

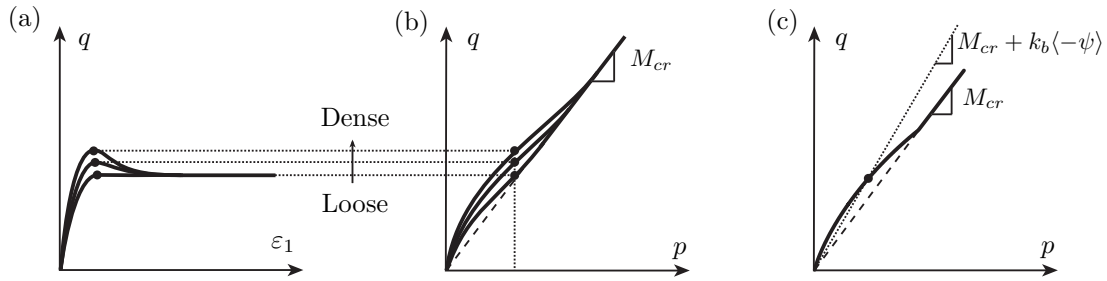

Figure 3. Typical variation of drained shear strength with isotropic pressure and relative density obtained from triaxial compression tests. (a) (ε_1, q)-diagram (b) (p, q)-diagram (Cambridge diagram) (c) Model formulation of bounding line.

The peak shear strength can be divided into two components. A base component is related to the critical state shear stress, with sand particles being able to rearrange under constant volume. This component can be represented by the critical stress ratio, M_{cr}. The second component arises from the dilation of the sand due to shearing. A densely packed sand will exhibit strong dilation and thus obtain a large shear strength due to the increased amount of energy needed for grain particles to slide around adjacent particles. The resulting peak shear strength can be defined by a threshold in stress space referred to as *failure envelope* or *bounding line*.

Since the location of the bounding line is highly correlated to the dilatancy, and thereby the packing density of the sand, it is meaningful to adopt the state parameter ψ in a bounding line formulation for constitutive modelling. The bounding line adopted by the current model is based on a formulation whereby the *bounding stress ratio*, $M_b = q/p$, is equal to M_{cr} plus a contribution proportional to ψ [32, 23]

$$M_b(\psi) \quad = \quad M_{cr} + k_b\langle -\psi \rangle \tag{3}$$

in which k_b is a dimensionless model parameter and $\langle\ \rangle$ refer to Macauley brackets, defined by $\langle x \rangle = 0$ if $x < 0$ else $\langle x \rangle = x$. This formulation ensures an increased peak shear strength for densely packed sands with curvature of the bounding line arising from the p-dependency of ψ.

Furthermore, the formulation ensures that the bounding line coincides with the critical state line for either very loose sands or at high isotropic pressures. The bounding line formulation is illustrated in Figure 3c.

It can be noted, that if the slope of the critical state line is very small (i.e. $\lambda \approx 0$), then the p-dependency of ψ in (1) become negligible. In this case, the location of the bounding and characteristic surfaces is then only influenced by the current void ratio, or as commonly adopted for sands, the relative density.

4. TRANSITION FROM COMPACTIVE TO DILATIVE BEHAVIOUR

Shearing of a granular material causes volumetric changes that are either compactive or dilative. Typical effective stress paths obtained from three triaxial compression tests on dense sand, performed with p = constant, are outlined in figure 4a. The corresponding volumetric changes are outlined in Figure 4b. The points, marked with dots, indicate the transition from compressive to dilative behaviour determined by $\delta\varepsilon_v/\delta\varepsilon_1 = 0$. These points indicate that there is a threshold in stress space, dividing the volumetric behaviour from compressive to dilative. This threshold is referred to as the *characteristic state* [22]. A consistent definition of the characteristic state is based on zero change in plastic volumetric strain, $d\varepsilon_v^p = 0$ [26].

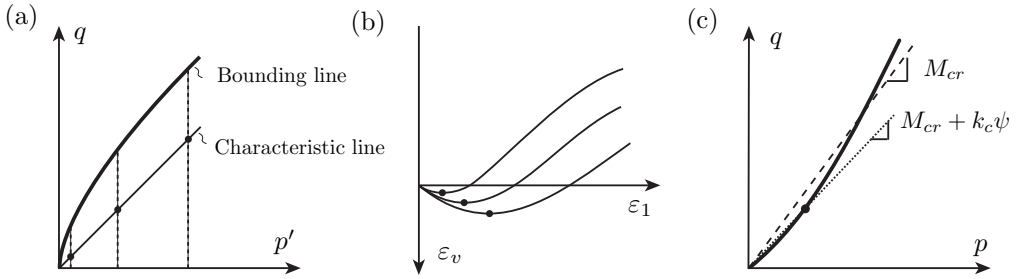

Figure 4. Outline of typical triaxial compression tests on dense sand performed with p' = constant. [16]

From monotonic triaxial tests, it has been determined that characteristic states can be represented by a straight line through origin in stress space [12, 15]. This line is referred as the *characteristic line*. Experiments indicate that the inclination of the characteristic line is constant and independent of both relative density and the isotropic stress level [12, 26]. Thus, it is tempting to define the characteristic line as a straight line with constant inclination, in terms of the *characteristic stress ratio*, $M_c = q/p$. However, while this is valid for monotonic loading, it may not be valid for cyclic loading. Also, one must have that $M_c \to M_{cr}$ as $\psi \to 0$, since the criterion defining the characteristic line, $d\varepsilon_v^p = 0$, must be fulfilled at the critical state. Thus, in the current model, the characteristic line is defined by

$$M_c(\psi) \quad = \quad M_{cr} + k_c\psi \tag{4}$$

in which k_c represents a dimensionless model parameter [23]. The characteristic line is illustrated in Figure 4c. The underlying physical background is rather weak, however, the simple formulation has been successfully adopted to simulate sand subjected to cyclic loading [23, 24].

5. MULTI-AXIAL FORMULATION

Granular materials exhibit a strong influence of the third stress invariant. This influence appear when comparing triaxial compression and extension tests, ie. lower shear friction can be sustained in triaxial extension. Thus, accurate simulation of granular materials require that the bounding and characteristic lines, defined in (3) and (4) respectively, are generalized to *bounding* and *characteristic surfaces* defined stress space using a multi-axial formulation. The multi-axial formulation introduced in this paper differs from the formulation used in the original model by Manzari *et al.* [23].

The influence of third stress invariant is conveniently depicted in the π-plane in which p remains constant. The minimum requirement for defining a contour in the π-plane is the specification of a 'corner' and a 'midpoint' of the triangular shape, corresponding to eg. triaxial compression and extension, respectively. Thus, for triaxial extension we may define the stress ratios of the bounding and characteristic lines similar to triaxial compression in (3) and (4) by

$$M_b^{ex} = M_{cr}^{ex} + k_b^{ex}\langle -\psi \rangle \qquad\qquad M_c^{ex} = M_{cr}^{ex} + k_c^{ex}\psi \tag{5}$$

in which M_{cr}^{ex}, k_b^{ex} and k_c^{ex} are model parameters for triaxial extension equivalent to the parameters M_{cr}, k_b and k_c for triaxial compression.

Several mathematical formulations are proposed to define the triangular contour of the bounding surface, e.g. Lade [11], Matsuoka-Nakai [14] and Mohr-Coulomb. A versatile shape formulation, derived from a cubic polynomial of principal stresses, is proposed by Krenk [20, 21]. The formulation prescribes a family of smooth and convex contours given in terms of

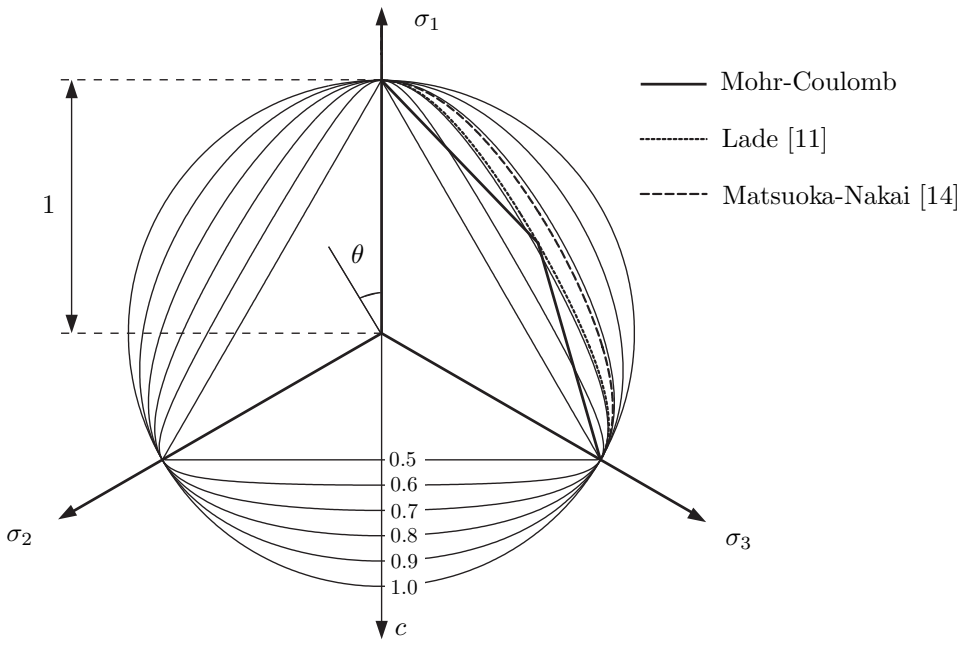

Figure 5. The family of surface contours prescribed by the function $g(c, \theta)$.

the second and third deviatoric stress invariants. The contours of this family can represent any shape from circular to triangular depending on a shape parameter. The original formulation by Krenk [20, 21] can be reformulated in terms of the Lode angle θ and the normalized shape function $g(c, \theta)$, defined such that $g(c, 0) = 1$ in triaxial compression and $g(c, \pi) = c$ in triaxial extension and thereby that $M_c^{ex} = cM_c$. In this case, g is expressed by

$$g(c,\theta) = \frac{\cos(\gamma)}{\cos\left(\frac{1}{3}\arccos(\cos(3\gamma)\cos(3\theta))\right)} \quad , \quad \gamma = \frac{\pi}{3} + \arctan\left(\frac{1-2c}{\sqrt{3}}\right) \tag{6}$$

The shape of the contours is uniquely defined by c. For example, a triangle is obtained for $c = 0.5$ whereas a circle is obtained for $c = 1$. The family of curves for $c \in [0.5; 1.0]$ is illustrated in Figure 5.

The shape of the bounding and characteristic surfaces are defined in terms of $g(c, \theta)$ in (6) using the shape parameters, $c = c_b$ and $c = c_c$, respectively. The values of c_b and c_c may be evaluated from the stress ratios defined in (3), (4) and (5).

$$c_b(\psi) = \frac{M_b^{ex}}{M_b} \qquad c_c(\psi) = \frac{M_c^{ex}}{M_c} \tag{7}$$

Both c_b and c_c are functions of ψ. For cohesionless granular materials, it is generally accepted that the bounding surface contour is triangular with $M_b \geq M_b^{ex}$; c_b will therefore lie in the range between 0.5 and 1. Representative values of c_c are limited accounted for in the literature.

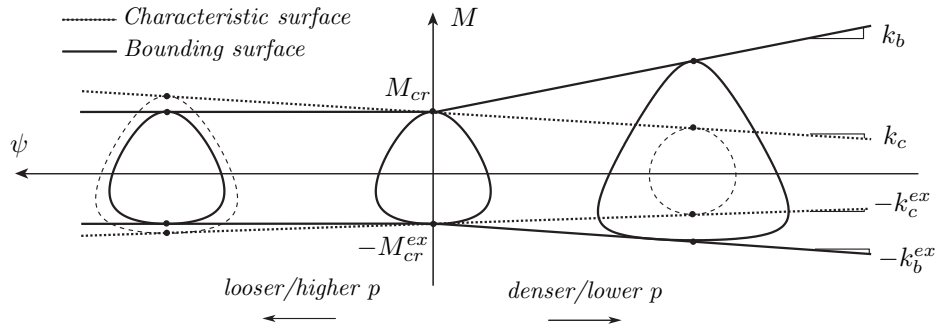

Figure 6. Visualization of the bounding and characteristic surface contours, as function of the state parameter ψ.

Figure 6 illustrates the shape of the bounding and characteristic surfaces as function of ψ as expressed in (7). For samples denser than critical ($\psi < 0$), the bounding surface obtains a triangular shape enclosing the characteristic surface; dilation will therefore occur before the bounding surface is reached. The bounding and characteristic surfaces become identical and equal to the *critical state surface* at the critical state ($\psi = 0$) where $c_b = c_c = M_{cr}^{ex}/M_{cr}$. For samples looser than critical ($\psi > 0$), the characteristic surface expands beyond the bounding surface to cause an entirely compactive behaviour, since the stress state always stays within the bounding surface.

Figure 7 illustrates the bounding surface in the principal stress space obtained using the expressions (3) and (5) in conjunction with (6) and (7).

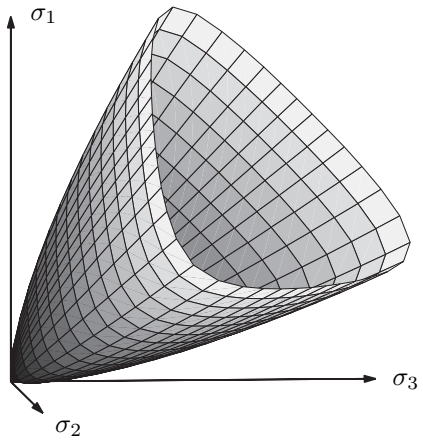

Figure 7. Visualization of the bounding surface in principal stress space.

A total of 6 model parameters define the surface contours and these may be determined from triaxial tests in both extension and compression. However, it may be appropriate to to adopt some simplifying assumptions in order to eliminate the model parameters M_{cr}^{ex}, k_b^{ex} and k_c^{ex} defining the behaviour in triaxial extension. Experimental evidence suggest that the critical angle of friction ϕ_{cr} is approximately equal under triaxial compression and extension [8]. Similarly, the widely applied Mohr-Coulomb failure criteria assumes that shear strength is governed by a constant angle of friction ϕ. The value of M is related to ϕ by $M = 6\sin\phi/(3-\sin\phi)$ in triaxial compression and $M^{ex} = 6\sin\phi/(3+\sin\phi)$ in triaxial extension. Combining these equations yields that the value of M and M^{ex} are related by $M^{ex} = 3M/(3+M)$. Thus, if the assumption of a constant friction angle under triaxial compression and extension is adopted, then (7) can be substituted by

$$c_b(\psi) = \frac{3}{3+M_b} \qquad c_c(\psi) = \frac{3}{3+M_c} \tag{8}$$

to eliminate the model parameters M_{cr}^{ex}, k_b^{ex} and k_c^{ex}.

If the assumption of a constant friction angle under triaxial compression and extension is undesired, then an alternative approach eliminating the 2 model parameters, k_b^{ex} and k_c^{ex}, may be done by simply choosing

$$c_b = c_c = \frac{M_{cr}^{ex}}{M^{cr}} \tag{9}$$

6. ELASTO-PLASTIC FORMULATION

The mathematical formulation of the plasticity model is presented in this section. The derivation follows that of Manzari and Prachathananukit [24]. The plasticity model is derived within the framework of non-associated elasto-plasticity. In the following derivation, all stress

notations refer to effective stresses. Bold symbols symbolize symmetric second-order tensors and the operators $\boldsymbol{u} : \boldsymbol{v}$ and $|\boldsymbol{u}|$ refer to the tensor product and tensor norm, respectively.

6.1. Elastic behaviour

The constitutive relations are formulated in terms of isotropic and deviatoric stress defined by $p = (\sigma_{11} + \sigma_{22} + \sigma_{33})/3$ and $\mathbf{s} = \boldsymbol{\sigma} - p\mathbf{I}$, respectively. $\mathbf{I}$ denotes the second order identity tensor. The elastic behaviour is based on the traditional isotropic hypoelastic formulation in which the elastic incremental stress-strain behaviour is defined by

$$d\boldsymbol{\varepsilon}_d^e = \frac{1}{2G} d\mathbf{s} \qquad\qquad d\varepsilon_v^e = \frac{1}{K} dp \tag{10}$$

where $d\boldsymbol{\varepsilon}_d^e$ and $d\varepsilon_v^e$ refer to the deviatoric and volumetric elastic strain increments, respectively. In the hypoelastic formulation, the elastic moduli, K and G, are assumed functions of the isotropic pressure

$$K = K_0 \left(\frac{p}{p_{\text{ref}}} \right)^b \qquad\qquad G = G_0 \left(\frac{p}{p_{\text{ref}}} \right)^b \tag{11}$$

in which p_{ref} is used as the reference pressure for which $K = K_0$ and $G = G_0$. The pressure exponent b is a model parameter, expressing the variation of the elastic modules with the isotropic pressure. The value of b is reported to vary from 0.435, at very small strains, to 0.765, at very large strains [33]. A value of 0.5 captures most of the important features of increased shear stiffness with pressure [34].

6.2. Yield and plastic potential functions

The elastic domain is enclosed by a yield surface with a cone-type shape and the apex in origin as illustrated in Figure 8. The yield surface is uniquely defined by the equation

$$f = |\mathbf{r}| - \sqrt{\frac{2}{3}} mp = 0 \qquad\qquad \mathbf{r} = \mathbf{s} - p\boldsymbol{\alpha} \tag{12}$$

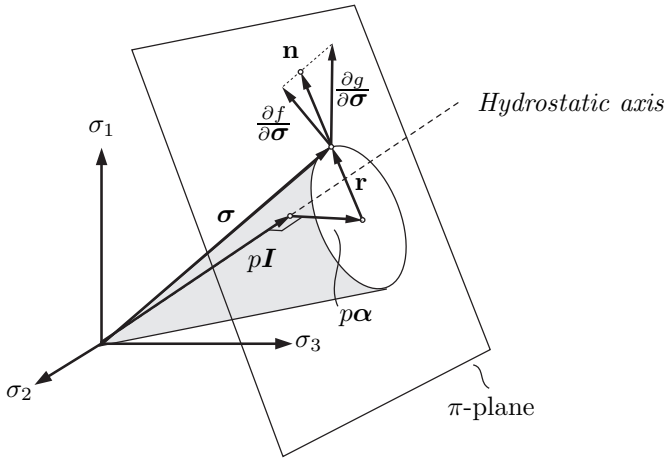

Figure 8. The cone-type yield surface defined in terms of m and $\boldsymbol{\alpha}$.

where $\boldsymbol{\alpha}$ is refered to as the deviatoric back-stress ratio tensor. This definition implies that the yield surface remains circular in the π-plane. The value $\sqrt{2/3}m$ and $\boldsymbol{\alpha}$ define the radius and the axis direction of the cone, respectively. The normals to the yield surface ($\partial f/\partial \boldsymbol{\sigma}$) and the plastic potential ($\partial g/\partial \boldsymbol{\sigma}$) define the loading and plastic flow direction, respectively. These are defined by:

$$\frac{\partial f}{\partial \boldsymbol{\sigma}} = \mathbf{n} - \frac{1}{3}N\mathbf{I} \qquad\qquad \frac{\partial g}{\partial \boldsymbol{\sigma}} = \mathbf{n} + \frac{1}{3}D\mathbf{I} \tag{13}$$

where $\mathbf{n} = \mathbf{r}/|\mathbf{r}|$ is the deviatoric normal to the yield surface. The parameters N and D define the magnitude of the isotropic components. From (12), it follows that $N = \boldsymbol{\alpha} : \mathbf{n} + \frac{2}{3}m$. The *dilatancy parameter* D has an important role as it controls the isotropic flow direction and thus the volumetric behaviour of the plasticity model. The plastic flow is non-associated, except in the special case where $D = -N$. It should be noted, that the formulation is not suitable for modeling constant stress-ratio response, i.e. consolidation paths where the stress ratio is constant as very high stress levels may be reached without inducing plastic strains, due to the lack of a surface cap.

6.3. Surface definitions using image points

The model is formulated by use of *image points*. The image point defines a point on a surface in the π-plane and is uniquely defined by the image vector $\boldsymbol{\alpha}_i$ pointing from the hydrostatic axis to the image point, in the direction of $\mathbf{n}$, see Figure 9. The bounding and characteristic surfaces, defined previously, can be formulated in terms of image vectors. In this case, the surfaces are expressed by

$$\boldsymbol{\alpha}_i = \sqrt{\frac{2}{3}}\left(g(c_i, \theta_{\mathbf{n}})M_i(\psi) - m\right)\mathbf{n} \quad , \quad i = b, c \tag{14}$$

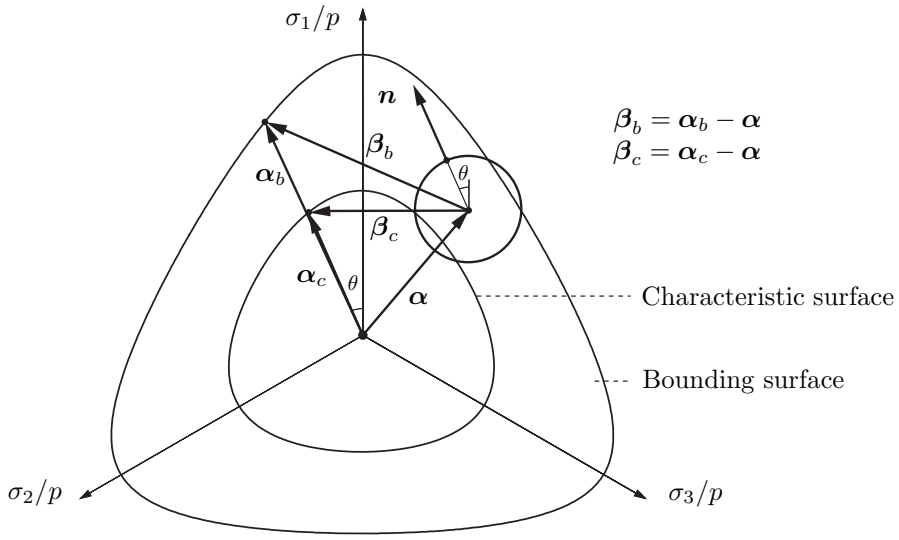

Figure 9. Illustration of the yield, characteristic and bounding surfaces in the π-plane.

where $\theta_{\mathbf{n}}$ refers to the Lode angle of $\mathbf{n}$. It is important to note that this surface formulation refers to back-stress ratios rather than stress ratios since the radius of the yield surface $\sqrt{2/3}m$ is subtracted. The Lode angle may be determined from the stress invariants J_2 and J_3 of $\mathbf{n}$

$$\cos(3\theta_n) = \frac{3\sqrt{3}}{2}\frac{J_3}{(J_2)^{3/2}} \tag{15}$$

The tensors, $\boldsymbol{\beta}_b = \boldsymbol{\alpha}_b - \boldsymbol{\alpha}$ and $\boldsymbol{\beta}_c = \boldsymbol{\alpha}_c - \boldsymbol{\alpha}$, define the distance between $\boldsymbol{\alpha}$ and their respective image points. These tensors are adopted in the formulation of model dilatancy and evolution laws for hardening parameters.

6.4. Volumetric behaviour

It is essential that the volumetric behaviour is simulated correctly. From (13), it follows that the plastic volumetric strains are proportional to D. The formulation of D is therefore of great importance. D is defined by

$$D = (A_0 + A_z)(\boldsymbol{\beta}_c : \mathbf{n}) \quad , \quad A_z = \langle \mathbf{z} : \mathbf{n} \rangle \tag{16}$$

where the *dilatancy parameter* A_0 represents a positive and dimensionless scaling parameter. This definition implies that the sign of $\boldsymbol{\beta}_c : \mathbf{n}$ defines the threshold between compressive and dilative behaviour. Thus, any stress state inside the characteristic surface obtains a compressive behaviour, since $\boldsymbol{\beta}_c : \mathbf{n} > 0$, whereas on-loading beyond the characteristic surface obtains a dilative behaviour, since $\boldsymbol{\beta}_c : \mathbf{n} < 0$.

The *unloading dilatancy parameter* A_z is defined in terms of the *fabric tensor* $\mathbf{z}$ which enables the model to capture the dilatancy of sand under reversed loading. The definition of A_z imply that $A_z = 0$, except during reversed loading where $A_z > 0$. The evolution of $\mathbf{z}$ is defined from an evolution law originally introduced by Dafalias [5]

$$d\mathbf{z} = \widetilde{\mathbf{z}} d\lambda \qquad \widetilde{\mathbf{z}} = -C_z(A_z^{max}\mathbf{n} + \mathbf{z})\langle -D \rangle \tag{17}$$

The factors C_z and A_z^{max} are positive dimensionless model parameters. The definition of $\mathbf{z}$ may be hard to interpret, however, the introduction of $\mathbf{z}$ enables the model to recall load history and evolve accordingly. The parameter A_z^{max} becomes an upper threshold value of A_z. The definition in (17) implies that $\mathbf{z}$ evolves in a direction opposite to $\mathbf{n}$ whenever the sample dilates ($D > 0$) such that the tensor product $\mathbf{z} : \mathbf{n}$ becomes positive, only when the load direction shifts to unloading.

6.5. Kinematic and isotropic hardening

Both kinematic and isotropic hardening are adopted in the model. The kinematic evolution law is based on a proposition by Dafalias and Popov [4]

$$d\boldsymbol{\alpha} = \widetilde{\boldsymbol{\alpha}} d\lambda \qquad \widetilde{\boldsymbol{\alpha}} = C_\alpha \left(\frac{|\boldsymbol{\beta}_{\mathbf{b}} : \mathbf{n}|}{b_r - |\boldsymbol{\beta}_b : \mathbf{n}|} \right) \boldsymbol{\beta}_b \tag{18}$$

C_α is a positive model parameter and b_r is a parameter that must be defined such that $b_r > |\boldsymbol{\beta}_b : \mathbf{n}|$. The adopted value is $b_r = 2\sqrt{2/3}(M_b - m)$. The evolution law ensures that $\boldsymbol{\alpha}$, the center of the yield cone, evolves in the direction of $\boldsymbol{\beta}_b$. The rate of evolution will converge to zero as $\boldsymbol{\alpha}$ approaches the bounding surface, due to inclusion of the factor $|\boldsymbol{\beta}_{\mathbf{b}} : \mathbf{n}|$. This implies

that the stress state remains inside the bounding surface during hardening. The bounding surface will contract during softening as the sand dilates and $\psi \to 0$. This contraction can leave the stress state outside the bounding surface. In this case, the direction of $\boldsymbol{\beta}_b$ is opposite to the loading direction $\mathbf{n}$, causing $|\boldsymbol{\beta}_b : \mathbf{n}|$ to become negative. Thus, $\boldsymbol{\alpha}$ will evolve in the opposite direction of $\boldsymbol{\beta}_b$ and thereby follow the contracting bounding surface. The isotropic hardening law is based on an original proposition by Manzari et al. [23]

$$dm = \widetilde{m} d\lambda \qquad \widetilde{m} = C_m(1 + e_0)D \tag{19}$$

where C_m is a model parameter and e_0 is the initial void ratio. The formulation implies that the evolution of m becomes proportional to the plastic rate of change of volume. This ensures that a compacted sand obtains a larger elastic domain than a loose sand. Even though the model allows for isotropic hardening, this model practically retain a constant radius m of the elastic domain. Therefore, isotropic hardening is often neglected ($C_m = 0$) since it is of less importance for the shear behaviour of sands.

6.6. Model parameters

A complete list of model parameters is given in Table I. The table include suggestions for elimination of several model parameters to ease calibration if limited data is available. Specification of initial conditions is required - these include e_0, p_0, $\mathbf{S}_0$, $\mathbf{A}_0$ and m_0. The initial value of the back-stress may conveniently be chosen as $\mathbf{A}_0 = \mathbf{S}_0/p_0$. It may be appropriate to choose a small initial size of the yield cone, i.e. $m_0 \approx 0.05$, and neglect isotropic hardening

List of model parameters:			Reduction of parameters	
Parameter		Description	Optional	Monotonic
Elasticity	K_0	Reference bulk modulus. [Pa]	-	-
	G_0	Reference shear modulus. [Pa]	$0.5 \times K_0$	-
	b	Pressure exponent.	0.5	-
Critical state	λ	Slope of CSL in e-ln(p) space.	-	-
	Γ	Critical state void ratio for p'=1Pa.	-	-
	M_{cr}	Slope of CSL in p-q space in triaxial compression.	-	-
	M_{cr}^{ex}	Slope of CSL in p-q space in triaxial extension.	n.a.[1]	-
Surface definitions	k_b	Bounding line in triaxial compression.	-	-
	k_b^{ex}	Bounding line in triaxial extension.	n.a.[1]	-
	k_c	Characteristic line in triaxial compression.	-	≈ 0
	k_c^{ex}	Characteristic line in triaxial extension.	n.a.[1]	≈ 0
Hardening	C_m	Evolution of isotropic hardening.	0	n.a.
	C_α	Evolution of kinematic hardening.	-	-
Dilatancy	A_0	Dilatancy parameter	-	-
Unloading dilatancy	C_z	Evolution of fabric tensor.	0	n.a.
	z_{max}	Limit size of fabric tensor.	0	n.a.
[1]: Simplifying assumption: $M_i^{ex} = 3M_i/(3 + M_i) \quad i = b, c$				

Table I. List of model parameters and optional parameter reductions.

($C_m = 0$). In this case, the size of the elastic domain remains small and the response to shearing is mainly governed by the evolution law for kinematic hardening. Thus, G_0 is of less importance and may conveniently be chosen as $G_0 = 0.5 \times K_0$ which corresponds to an elastic Poisson's ratio equal to 0.29. A representative shear stiffness is then obtained by calibrating C_α.

7. INTEGRATION ALGORITHM

An efficient and accurate time-stepping integration scheme must be adopted to incrementalize and utilize the cyclic plasticity model. The fact that the elasto-plastic stiffness depends on both current stresses and hardening parameters challenges the integration of the constitutive relations. The most suitable integration algorithm may depend on the type of global solver. This paper provides a fast, stable and accurate integration algorithm suitable for an explicit global solver, such as FLAC3D. It is characteristic for an explicit global solver, that the step-size is very small. This calls for a fast return mapping or sub-stepping integration scheme on constitutive level. A benchmark analysis by Manzari [24] included a cutting plane algorithm belonging to the family of explicit return mapping methodss, originally derived by Simo & Ortiz [29]. The benchmark analysis showed that the highest efficiency was obtained using the cutting plane algorithm, however, the algorithm failed to converge at low stress levels. A return mapping method is adopted in this paper and convergence problems are addressed by adopting a suitable implementation strategy.

7.1. Return mapping method

The derivation of the return mapping method relies on basic elasto-plastic assumptions. Firstly, the integration of the constitutive relations must satisfy the consistency condition. The consistency condition, in terms of the hardening parameter H, is given by

$$\frac{\partial f}{\partial \boldsymbol{\sigma}} d\boldsymbol{\sigma} - H d\lambda = 0 \qquad\qquad H = -\left(\frac{\partial f}{\partial \boldsymbol{\alpha}} \widetilde{\boldsymbol{\alpha}} + \frac{\partial f}{\partial m} \widetilde{m} \right) \tag{20}$$

Secondly, the theory of elasto-plasticity assumes that a stress increment can be divided into an elastic and a plastic part

$$\Delta\boldsymbol{\sigma} = \mathbf{C} : (\Delta\boldsymbol{\varepsilon} - \Delta\boldsymbol{\varepsilon}^p) = \Delta\boldsymbol{\sigma}^e - \Delta\boldsymbol{\sigma}^p \tag{21}$$

The stress increments $\Delta\boldsymbol{\sigma}^e$ and $\Delta\boldsymbol{\sigma}^p$ are referred to as the elastic predictor and plastic corrector, respectively and $\mathbf{C}$ refers to the hypoelastic stiffness matrix. The purpose of the return mapping method, is to determine the plastic corrector such that the stress state remains on the yield surface while the consistency condition is fulfilled. Given the current stress state $\boldsymbol{\sigma}_0$ and a strain increment $\Delta\boldsymbol{\varepsilon}$, the stress state in the subsequent step can be calculated by

$$\boldsymbol{\sigma} = \boldsymbol{\sigma}_0 + \mathbf{C} : (\Delta\boldsymbol{\varepsilon} - \Delta\boldsymbol{\varepsilon}^p) \tag{22}$$

according to (21). By initially setting $\Delta\boldsymbol{\varepsilon}^p = \mathbf{0}$ in (22), the elastic predictor stress $\boldsymbol{\sigma}^{elas}$ is calculated, leaving the plastic correction $\Delta\boldsymbol{\sigma}^p = \mathbf{C} : \Delta\boldsymbol{\varepsilon}^p$ to be determined. The plastic correction is governed by the flow rule

$$\Delta\boldsymbol{\varepsilon}^p = \Delta\lambda \frac{\partial g}{\partial \boldsymbol{\sigma}} \tag{23}$$

Thus, the purpose of the return mapping method is reduced to determining the magnitude of $\Delta\lambda$ while fulfilling (20). This is addressed by a first order Taylor expansion of the yield function around $\boldsymbol{\sigma}^{elas}$ while utilizing that $f(\boldsymbol{\sigma}) = 0$

$$f(\boldsymbol{\sigma}) = f(\boldsymbol{\sigma}^{elas}) - \frac{df}{d\boldsymbol{\sigma}} : \Delta\boldsymbol{\sigma}^p + \frac{df}{d\lambda}\Delta\lambda = 0 \tag{24}$$

From the consistency condition, it follows that $df/d\lambda = H$. Thus, by rearranging (24), and using the relation $\Delta\boldsymbol{\sigma}^p = \mathbf{C}\Delta\boldsymbol{\varepsilon}^p$ combined with (23), a linear expression determining the magnitude of the plastic multiplier can be obtained. This linear expression is however inadequate since the gradients $\partial f/\partial\boldsymbol{\sigma}$ and $\partial g/\partial\boldsymbol{\sigma}$ as well as the hardening parameter H vary along the return path from $\boldsymbol{\sigma}^{elas}$ to $\boldsymbol{\sigma}$. An iterative scheme must be adopted to solve this problem. Simo and Ortiz [29] proposed an explicit scheme, the general return mapping method, solving the problem in a sequence of linearized steps. The steps are given by

$$\boldsymbol{\sigma}_i = \boldsymbol{\sigma}_0 + \mathbf{C} : (\Delta\boldsymbol{\varepsilon} - \Delta\boldsymbol{\varepsilon}^p_{i-1}) \tag{25}$$

$$\Delta\lambda = \left(\frac{f(\boldsymbol{\sigma}_i)}{(\partial f/\partial\boldsymbol{\sigma}) : \mathbf{C} : (\partial g/\partial\boldsymbol{\sigma}) + H}\right)_{i-1} \tag{26}$$

$$\Delta\boldsymbol{\varepsilon}^p_i = \Delta\boldsymbol{\varepsilon}^p_{i-1} + \Delta\lambda\left(\frac{\partial g}{\partial\boldsymbol{\sigma}}\right)_{i-1} \tag{27}$$

$$\Delta\mathbf{x}_i = \Delta\mathbf{x}_{i-1} + \Delta\lambda\widetilde{\mathbf{x}}_{i-1} \tag{28}$$

where $\mathbf{x}$ refers to a hardening parameter and $\tilde{\mathbf{x}}$ is the corresponding evolution law. A geometric interpretation of the general return mapping method is illustrated in Figure 10.

It is convenient to rewrite the integration steps (25)-(28) in terms of model parameters. From (12) and (20), it follows that the hardening parameter H can expressed by

$$H = p(\mathbf{n} : \widetilde{\boldsymbol{\alpha}} + \sqrt{\frac{2}{3}}\widetilde{m}) \tag{29}$$

The second denominator term in (25) can be simplified by exploiting that stresses are divided in isotropic and deviatoric stresses. Thus, from (11) and (13), the second denominator term becomes

$$\frac{\partial f}{\partial\boldsymbol{\sigma}} : C : \frac{\partial Q}{\partial\boldsymbol{\sigma}} = -NDK + 2G \tag{30}$$

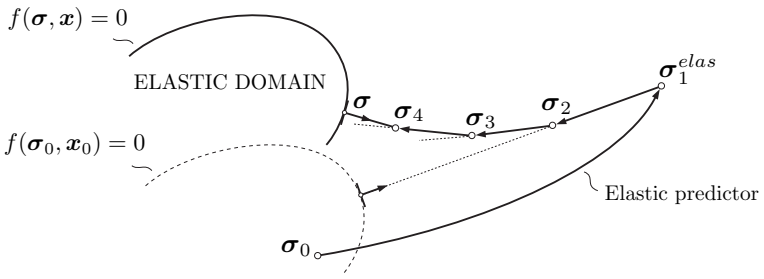

Figure 10. Geometric interpretation of the general return mapping method [29]. An elastic prediction brings the stress state from $\boldsymbol{\sigma}_0$ to $\boldsymbol{\sigma}_1^{elas}$. Subsequently, successive plastic correction steps are applied to return the stress state to the yield surface.

7.2. Integration of elastic relations

The integration of the elastic relations needs special attention due to the p-dependency of the bulk and shear modulus. The resulting isotropic stress p arising from the elastic increment $\Delta\varepsilon_v^e$ can be determined by integration of the elastic relation (11).

$$p = \left(p_0^{1-b} + \frac{1}{p_a^b}(1-b)K_0 \Delta\varepsilon_v^e \right)^{\frac{1}{1-b}} \tag{31}$$

p_0 denotes the isotropic stress at the previous step. The resulting bulk modulus can be calculated subsequently by $K = \Delta p / \Delta\varepsilon_v^e$, with $\Delta p = p - p_0$. If $\Delta\varepsilon_v^e = 0$, then K must be evaluated from (11). The shear modulus scales proportional to the bulk modulus, thus the

---

function ReturnMappingMethod$(\Delta\boldsymbol{\varepsilon}_d,\ \Delta\varepsilon_v)$

Initial state:

$\mathbf{s}_0,\ p_0,\ m,\ \boldsymbol{\alpha},\ \mathbf{z},\ \varepsilon_v,\ \Delta\boldsymbol{\varepsilon}_d^p = \mathbf{0},\ \Delta\varepsilon_v^p = 0$

Update void ratio:

$\varepsilon_v = \varepsilon_v + \Delta\varepsilon_v$

$e = e_0 - (1+e_0)\varepsilon_v$

Iterations $i = 1, 2, ..., i_{max}$

$p = \left(p_0^{1-b} + (K_0/p_a^b)(1-b)(\Delta\varepsilon_v - \Delta\varepsilon_v^p)\right)^{1/(1-b)}$

$\mathbf{s} = \mathbf{s}_0 + 2G(\Delta\boldsymbol{\varepsilon}_d - \Delta\boldsymbol{\varepsilon}_d^p)$

$\psi = e - (\Gamma - \lambda \ln(p/p_{\text{ref}}))$

If $f(p,\mathbf{s})/p > \epsilon_f$:

Update: $N,\ D,\ K,\ G,\ \mathbf{n},\ \widetilde{\boldsymbol{\alpha}},\ \widetilde{m},\ \widetilde{z}$

Add plastic correction:

$$\Delta\lambda = \frac{f(p,\mathbf{s})}{-NDK + 2G + p(\mathbf{n} : \widetilde{\boldsymbol{\alpha}} + \sqrt{2/3}\widetilde{m})}$$

$$\begin{aligned}
\Delta\boldsymbol{\varepsilon}_d^p &= \Delta\boldsymbol{\varepsilon}_d^p + \Delta\lambda\mathbf{n} \\
\Delta\varepsilon_v^p &= \Delta\varepsilon_v^p + \Delta\lambda D \\
\boldsymbol{\alpha} &= \boldsymbol{\alpha} + \Delta\lambda\widetilde{\boldsymbol{\alpha}} \\
m &= m + \Delta\lambda\widetilde{m} \\
\mathbf{z} &= \mathbf{z} + \Delta\lambda\widetilde{\mathbf{z}}
\end{aligned}$$

Else:

$\mathbf{s}_0 = \mathbf{s}$

$p_0 = p$

return

Table II. The general return mapping method by [29] applied to the modified critical state two-surface plasticity model.

resulting shear stress can be evaluated by

$$\mathbf{s} = \mathbf{s}_0 + 2G\Delta\boldsymbol{\varepsilon}_d^e \qquad G = G_0 \begin{cases} K/K_0 & \text{if } \Delta\varepsilon_v^e \neq 0 \\ (p/p_a)^b & \text{if } \Delta\varepsilon_v^e = 0 \end{cases} \tag{32}$$

The model specific return mapping method, expressed by the above formulations, is outlined in Table II. Note that the return mapping algorithm will continue iterations until $\boldsymbol{\sigma}$ coincides with the yield surface which is evaluated by the criterion $f(p, \mathbf{s}) < \epsilon_f \times p$. Here, ϵ_f specifies a given tolerance. The criterium is chosen to scale proportional to p, since f is evaluated in terms of stress.

8. IMPLEMENTATION STRATEGY

A suitable implementation strategy must be adopted to ensure robustness and efficiency of the integration scheme before actual coding of the plasticity model for computer application. The general return mapping method is only conditionally stable when adopted for the two-surface critical state plasticity model. In general, the return mapping method fails to converge if the imposed strain increment becomes too large. These convergence problems increase as $p \to 0$.

In this paper, most convergence problems are solved by strain-controlled sub-stepping. In general, the imposed increments should be sufficiently small so that sub-stepping on constitutive level is avoided. However, if the isotropic stress level in a single element approaches zero, then extremely small increments must be enforced at the global level to obtain a stable solution. Instead of enforcing a fixed increment size, the local increments are divided into a number of sub-steps as required. The size of each sub-increment is continuously updated from a specified tolerance criterion, so that only the necessary number of sub-increments are applied.

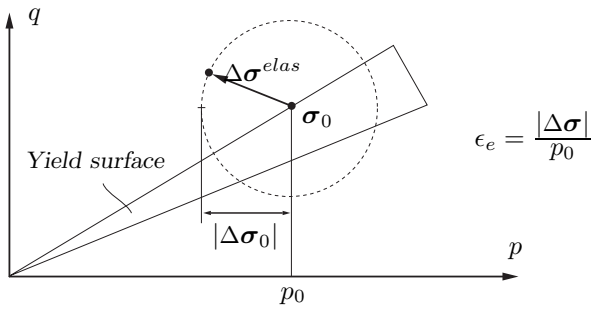

Figure 11. Criterion for initiating a sub-step illustrated in the $p - q$ stress plane

The active sub-step control uses a tolerence criterion based on the magnitude of the elastic prediction $\Delta\boldsymbol{\sigma}^{elas}$, as shown in Figure 11. If the magnitude of the elastic prediction exceeds a given tolerance, the increment is then divided into two sub-increments. The elastic prediction is estimated from the elasticity in the initial state, i.e. $G = G(\boldsymbol{\sigma}_0)$ and $K = K(\boldsymbol{\sigma}_0)$. The criterion initiating sub-steps is defined by $|\Delta\boldsymbol{\sigma}|/p_0 > \epsilon_{\mathrm{e}}$, with ϵ_{e} specifying a given tolerance. The criterion scales proportional to the isotropic pressure, thus sub-steps are initiated mainly at low stress levels.

The introduction of increment controlled sub-steps ensures that the return-mapping method remains stable. However, the number of sub-steps grows drastically as $p \rightarrow 0$. The high computational costs may be significantly reduced using a stress correction strategy as $p \rightarrow 0$. Here, a stress correction is introduced to prevent p to exceed a lower limit given by $p_{\mathrm{m}} = \epsilon_{\mathrm{m}} p_{\mathrm{ref}}$, in which ϵ_{m} is a specified tolerance criteria. Note that the reference pressure p_{ref} is a constant and may for example be chosen equal to the atmospheric pressure.

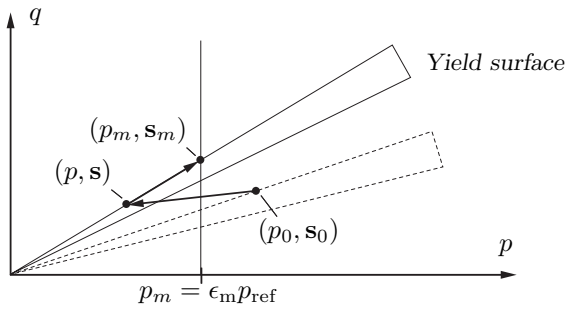

Figure 12. Stress correction for $p \rightarrow 0$ illustrated in the $p - q$ stress plane.

The value of p_m is chosen such that $p_m << p_{\mathrm{ref}}$. If p obtains a value less than p_{m}, then the soil matrix is practically liquefying. In this case, scaling may be applied to translate the stress state from $(p, \mathbf{s})$ to $(p_m, \mathbf{s}_m)$, as illustrated in Figure 12.

$$p_m = \epsilon_{\mathrm{m}} p_{\mathrm{ref}} \qquad \mathbf{s}_m = \left(\frac{p_m}{p} \right) \mathbf{s} \tag{33}$$

This correction strategy may be adopted to significantly reduce the computational costs as cyclic liquefaction evolve. The correction clearly violates the underlying model formulation. However, the correction only slightly changes the model response and may be justified, since validity of the assumptions used to formulate the plasticity model are rather weak for $p \rightarrow 0$. When the correction is applied, the value of $\mathbf{z}$ is simultaneously set to zero ($\mathbf{z} = \mathbf{0}$) since the soil matrix is liquefying. Setting $\mathbf{z}$ to zero effectively resets the ability of the model to recall load history.

Numerical instability occurs if the radius of the yield surface becomes zero or negative ($m \leq 0$). This can occur since the radius of the yield surface is defined to decrease proportionally to the rate of volumetric expansion. Instability can be avoided by setting $\tilde{m} = 0$ in the case where $0 > C_m(1 + e_0)D$ and $m < m_l$. The constant m_l represents a specified lower bound for the size of the yield surface.

An algorithm combining the above mentioned correction strategies is outlined in Table III.

9. EFFICIENCY, ACCURACY AND STABILITY

The performance of the integration scheme is investigated for efficiency, stability and accuracy on a constitutive level. Simulations of conventional cyclic and monotonic triaxial tests,

Initial state:

$\mathbf{s}_0,\ p_0,\ \varepsilon_v,\ m,\ \boldsymbol{\alpha},\ \mathbf{z}$

$\zeta = 0,\ k = 1$

$\Delta\boldsymbol{\varepsilon}_{d,0},\ \Delta\varepsilon_{v,0}$

Iterations $j = 1, 2, ..., j_{max}$

$\Delta\varepsilon_v = \Delta\varepsilon_{v,0}/k$

$\Delta\boldsymbol{\varepsilon}_d = \Delta\boldsymbol{\varepsilon}_{d,0}/k$

$\Delta\boldsymbol{\sigma}^{elas} = \left(2G_0\Delta\boldsymbol{\varepsilon}_d + K_0\mathbf{I}\Delta\varepsilon_v\right)\left(p_0/p_r\right)^b$

If $|\Delta\boldsymbol{\sigma}^{elas}|/p_0 > \epsilon_{\mathrm{e}}$*: Reduce step-length*

$k = 2k$

Else: Start integration

$[s_0,\ p_0] = \mathbf{ReturnMappingMethod}(\Delta\boldsymbol{\varepsilon}_d,\ \Delta\varepsilon_v)$

If $p_0 < \epsilon_{\mathrm{m}} p_{\mathrm{ref}}$*: Add stress correction*

$\mathbf{s}_0 = \epsilon_{\mathrm{m}}(p_{\mathrm{ref}}/p_0)\mathbf{s}_0$

$p_0 = \epsilon_{\mathrm{m}} p_{\mathrm{ref}}$

$\mathbf{z}_0 = \mathbf{0}$

$\zeta = \zeta + 1/k$

Stop iterations when $\zeta = 1$

Final state: $\boldsymbol{\sigma}_0,\ p_0,\ \varepsilon_v,\ m,\ \boldsymbol{\alpha},\ \mathbf{z}$

Table III. Implementation strategy applied to obtain a stable numerical integration scheme

performed in undrained conditions ($\Delta\epsilon_v = 0$), are used for analysis. The adopted model parameters are similar to the parameters used for simulation of Nevada Sand [23, 24]. These are listed in Table IV.

$K_0 = 31.4$MPa	$M_c = 1.1$	$k_b = 4.0$	$A_0 = 2.64$
$G_0 = 31.4$MPa	$\lambda = 0.025$	$k_c = 4.2$	$A_z^{max} = 100$
	$e_r = 0.93$	$C_\alpha = 1200$	$C_z = 100$

Table IV. Model parameters adopted for analysis of efficiency, stability and accuracy.

First, the efficiency and accuracy of the integration scheme (Table II) is investigated. The analysis is based on simulations of monotonic and cyclic tests. The monotonic test simulates a loose sample with the initial confining stress $p = 100$kPa and void ratio $e_0 = 0.82$ while the cyclic test simulates a medium-dense sample with the initial confining stress $p = 150$kPa and void ratio $e_0 = 0.65$. The cyclic test is simulated with a constant shear stress offset ($q = 35 \pm 25$kPa) in order to avoid stability problems when $p \to 0$. The simulations are illustrated in Figure 13.

The accuracy of the return mapping method is evaluated in terms of an error measure

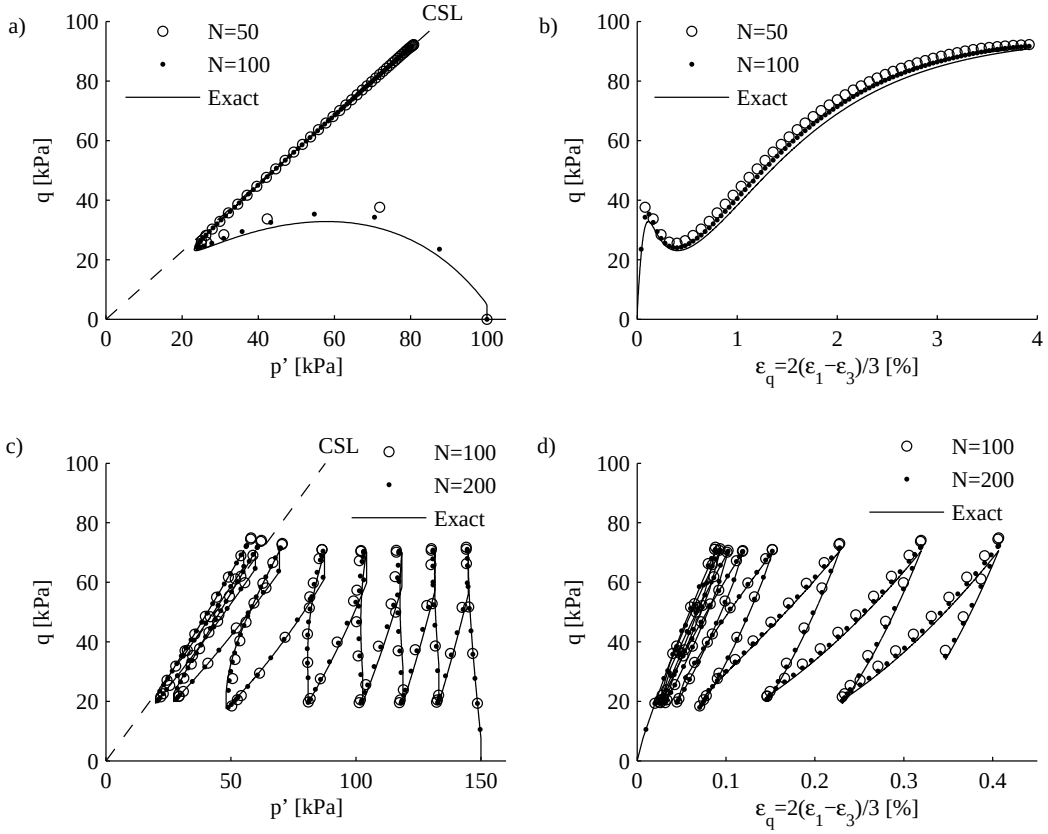

Figure 13. Illustration of simulations used to investigate the accuracy and efficency of the integration scheme. a-b) Monotonic loading. c-d) Cyclic loading

defined by

$$error = \frac{1}{p_{\text{ref}}} \left(\frac{1}{N} \sum_{i=1}^{N} |\boldsymbol{\sigma}_i - \boldsymbol{\sigma}_{i,exact}| \right) \tag{34}$$

where N is the number of steps and $\boldsymbol{\sigma}_{exact}$ refers to the exact solution approximated by simulations having a very small step size. The reference pressure is chosen as $p_{\text{ref}} = 100$kPa. The accuracy is investigated as a function of the imposed strain increments $\Delta\epsilon$ and the resulting step size is quantified in terms of the ratio $\Delta(q/p)_1$ of the initial step. For example, if $\Delta(q/p)_1 = 1.1 = M_{cr}$, then the critical stress ratio is reached in only one step. The results of the simulations are listed in Table V. They indicate that the computational expense, evaluated in terms of total iterations, increases proportional to N. Thus, independent of step length, approximately 2 iterations are on average required at each step. The error decreases potentially with N, see Figure 14a, and proportional to the ratio $\Delta(q/p)_1$, see Figure 14b. The results suggest that a reasonable accuracy, say $error < 2-3\%$, is obtained when the step size is chosen so that $\Delta(q/p)_1 < 0.1$. The tolerance criteria ϵ_f has an influence on efficiency

No.	Loading type	N	$\Delta\varepsilon_1$	$\Delta(q/p)_1$	Iterations	error [%]
1	Monotonic	50	8×10^{-4}	0.52	103	6.2
2	Monotonic	100	4×10^{-4}	0.27	207	3.1
3	Monotonic	200	2×10^{-4}	0.14	413	1.6
4	Monotonic	500	1×10^{-4}	0.066	1023	0.63
5	Monotonic	1000	4×10^{-5}	0.038	2027	0.31
6	Monotonic	5000	8×10^{-6}	0.0075	9794	0.057
7	Cyclic	100	2×10^{-4}	0.13	241	3.2
8	Cyclic	200	1×10^{-4}	0.071	465	1.4
9	Cyclic	500	4×10^{-5}	0.031	1089	0.57
10	Cyclic	1000	2×10^{-5}	0.015	2059	0.28
11	Cyclic	2000	1×10^{-5}	0.0077	3910	0.14
12	Cyclic	5000	4×10^{-6}	0.0031	9439	0.05

Table V. Analysis of accuracy and efficiency as function of step size. ($\epsilon_f = 10^{-4}$)

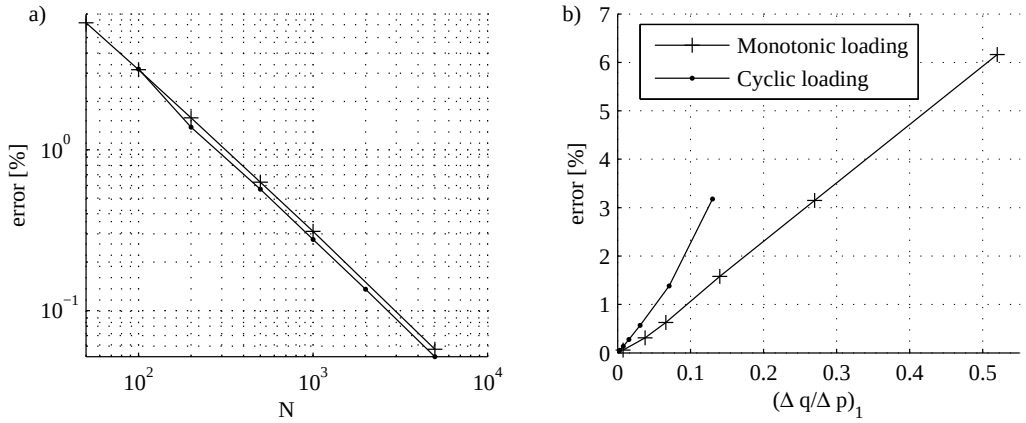

Figure 14. Error of return mapping algorithm as function of N and $\Delta(q/p)_1$.

and accuracy. Table VI lists the results of simulations performed in order to investigate the influence of ϵ_f. The results suggest that a value of $\epsilon_f = 10^{-4}$ is appropriate to optimize

No.	Loading type	ϵ_f	Iterations	ϵ [%]
1	Cyclic	10^{-8}	2725	0.33
1	Cyclic	10^{-6}	2374	0.33
2	Cyclic	10^{-5}	2259	0.33
3	Cyclic	10^{-4}	2059	0.33
4	Cyclic	10^{-3}	1850	0.42
5	Cyclic	10^{-2}	1691	3.3

Table VI. Influence of the tolerance criteria ϵ_f on efficiency and accuracy. The simulations are performed with N=1000 and $\Delta\varepsilon_1 = 2.5 \times 10^{-5}$

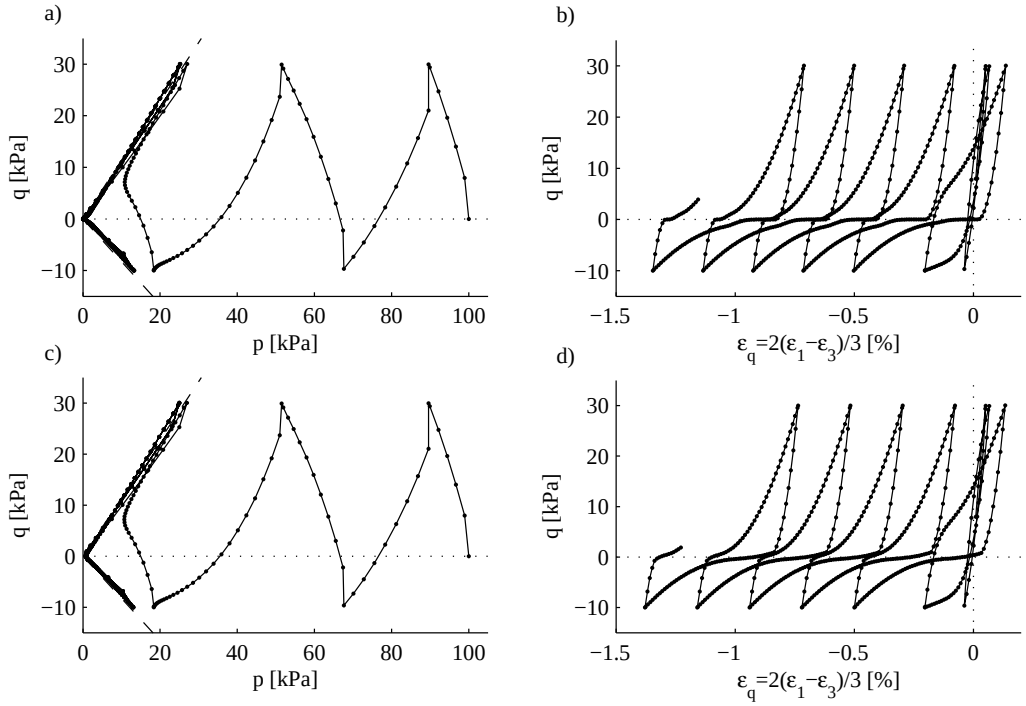

Figure 15. Simulation used in stability analysis. a-b) Simulation no. 6, c-d) Simulation no. 10

efficiency without loosing accuracy.

The stability of the integration scheme and implementation strategy (Table II and III) was tested by simulation of loose and dense samples subjected to a wide range of load histories. Here, an undrained cyclic triaxial test performed on a medium-loose sample ($e_0 = 0.75$) subjected to cyclic loading ($q = 10 \pm 20$kPa) is considered, see Figure 15a and 15b. The cyclic loading causes cyclic liquefaction, which is harsh from a numerical point of view, since $p \to 0$. The value of C_z is set to $C_z = 500$ in order to cause strong contraction during unloading and thereby challenging the stability of the algorithm. Series of simulations are performed to investigate the effect of N, ϵ_e and ϵ_m on stability. The results are listed in Table VII. The simulations 1-3 suggest that reducing the step-length is inappropriate to avoid numerical instability. Even a dramatic decrease in step-size does not ensure convergence. The simulations 4-8 show that the strain-controlled sub-stepping is sufficient in order to avoid numerical instability if the tolerance is chosen so that $\epsilon_{\mathrm{e}} \leq 0.3$. However, the stability is obtained at a relatively high computational cost (minimum 24856 iterations).

The computational costs may be significantly reduced if the stress correction for $p \to 0$ is adopted, ie. $\epsilon_{\mathrm{m}} > 0$. For example, if $\epsilon_{\mathrm{m}} = 0.01$, then the computational costs are reduced to only $3033/24856 = 12\%$. Thus, it may be desirable to adopt this correction strategy if cyclic liquefaction is expected to evolve over a large domain. The correction alters the model response as $p \to 0$, however only slightly. Figure 15c and 15d illustrate a simulation performed with $\epsilon_{\mathrm{m}} = 0.01$ which may be compared with the simulation in Figure 15a 15b performed without

No.	N	$\Delta\varepsilon_1$	ϵ_{e}	ϵ_{m}	Iterations
1	600	10^{-4}	-	-	*
2	6000	10^{-5}	-	-	*
3	60000	10^{-6}	-	-	*
4	600	10^{-4}	0.8	-	*
5	600	10^{-4}	0.5	-	*
6	600	10^{-4}	0.3	-	24856
7	600	10^{-4}	0.2	-	32289
8	600	10^{-4}	0.1	-	61453
9	600	10^{-4}	0.3	10^{-1}	1501
10	600	10^{-4}	0.3	10^{-2}	3033
11	600	10^{-4}	0.3	10^{-3}	5769
12	600	10^{-4}	0.3	10^{-4}	8281
13	600	10^{-4}	0.3	10^{-5}	15761
* No convergence					

Table VII. Results of stability analysis. ($\epsilon_f = 10^{-4}$)

correction for $p \to 0$.

To summarize, a sufficient accuracy of the return mapping method may be obtained if the step-size is chosen such that $\Delta(q/p)_1 < 0.1$ while a combination of $\epsilon_e = 0.3$ and $\epsilon_m = 10^{-2}$ may be a good compromise to ensure both efficiency and stability.

10. CONCLUSION

This paper provides comprehensive background information and documentation for the implementation of the modified critical state two-surface plasticity model as a user-subroutine in the commercial finite difference, FLAC3D by Itasca. The plasticity model is equal to the model by Manzari et al. but uses an alternative multi-dimensional surface formulation. The model parameters are discussed and suggestions for parameter reductions are made. A fast and accurate time-stepping integration scheme suitable for an explicit global solver is presented. The integration scheme is based on the general return mapping method, which is only conditionally stable. Convergence problems are addressed by adopting a suitable implementation strategy consisting of increment controlled sub-stepping. Other correction strategies are introduced, including a correction introduced to increase the efficiency as $p \to 0$. Finally, simulations are made to investigate the performance of the integration scheme and appropriate tolerance criteria are suggested to obtain sufficient efficiency, stability and accuracy. Thus, this paper provides complete information for the implementation of a robust user-defined constitutive model, capable of simulating the response of non-cohesive sands or silts, in a commercial finite element or finite difference code.

REFERENCES

1. Been K, Jefferies MG. A state parameter for sands. *Géotechnique* 1985; **35**(2):99-112
2. Casagrande, A. Characteristics of cohesionless soil affecting the stability of slopes and earth fills. *Journal of Boston Society of Civil Engineering* 1936; **23**(1):13-32
3. Crouch RS, Wolf J, Dafalias Y. Unified critical state bounding surface plasticity model for soil. *Journal of Engineering Mechanics* 1994; **120**(11):2251-2270
4. Dafalias YF, Popov EP. Plastic internal variable formalism of cyclic plasticity. *Journal of Applied Mechanics* 1976; **98**(4):645-650
5. Dafalias YF, Manzari MT. Modeling of fabric effect on the cyclic loading response of granular soils. *Proceedings of ASCE 13th Engineering Mechanics Conference*, Baltimore, Maryland, 13-16 June 1999
6. Dafalias YF, Manzari MT, Papadimitriou AG. SANICLAY: simple anisotropic clay plasticity model. *International Journal for Numerical and Analytical Methods in Geomechanics* 2006; **30**(12):1231-1257
7. Gajo A, Wood DM. A kinematic hardening constitutive model for sands: the multiaxial formulation. *International Journal for Numerical and Analytical Methods in Geomechanics* 1999; **23**(9):925-965
8. Gens, A. Stress-strain and strength of a low plasticity clay. *Ph.D. Thesis* Imperial College, London. 1982
9. De Groot MB, Bolton MD, Foray P, Meijers P, Palmer AC, Sandven R, Sawicki A, Teh TC. Physics of liquefaction phenomena around marine structures. *Journal of Waterway, Port, Coastal and Ocean Engineering* 2006; **132**(4):227-243.
10. Imam SMR, Morgenstern NR, Robertson PK, Chan DH. A critical-state constitutive model for liquefiable sand. *Canadian Geotechnical Journal* 2005; **42**(3):830-855.
11. Lade PV. Elasto-plastic stress-strain theory for cohesionless soil with curved yield surfaces. *International Journal of Solids and Structures* 1977. **13**:1019-1035
12. Lade PV, Ibsen LB. A study of the phase transformation and the characteristic lines of sand behaviour. *Deformation and progressive failure in Geomechanics.* IS-NAGOYA, 1997. Pergamon Press, 353-358
13. Li XS, Dafalias, YF. Dilatancy for cohesionless soils. *Géotechnique* 2000. **50**(4):449-460
14. Matsuoka H, Nakai T. Relationship among Tresca, Mohr-Coulomb and Matsuoka-Nakai failure criteria.*Soils and Foundations* 1985. **25**:123-128
15. Ibsen LB, Lade PV. The role of the characteristic line in static soil behavior. *4" Workshop on localisation and bifurcation theory for soils and rocks.* A.A.Balkema, 1998.
16. Ibsen LB. The mechanism controlling static liquefaction and cyclic strength of sand. *Workshop on the physics and mechanics of soil liquefaction.* A.A.Balkema, 1999.
17. Ibsen LB, Praastrup U. The danish rigid boundary true triaxial apparatus for soil testing. *Geotechnical testing journal* 2002; **25**(3):1-12.
18. Ishihara K, Tatsuoka F, Yasuda, S. Undrained deformation and liquefaction of sand under cyclic stresses. *Soils and Foundations* 1975; **15**(1):29-44.
19. Jefferies, M. G. Nor-Sand: a simple critical state model for sand. *Géotechnique* 1993; **43**(1):91-103.
20. Krenk S. Family of Invariant Stress Surfaces. *Journal of Engineering Mechanics - Proceedings of the ASCE* 1996; **122**(3):201-208.
21. Krenk S. Characteristic state plasticity for granular materials : Part I: Basic theory. *International Journal of Solids and Structures* 2000; **37**(43):6343-6360.
22. Luong MP. Stress-strain aspects of cohesionless soils under cyclic and transient loading. *International symposium on soil under cyclic and transient loading.* A.A.Balkema, 1982.
23. Manzari MT, Dafalias YF. Critical state two-surface plasticity model for sands *Géotechnique* 1997; **47**(2):255-272
24. Manzari MT, Prachathananukit R. On integration of a cyclic soil plasticity model *International Journal for Numerical and Analytical Methods in Geomechanics* 2001; **25**(6):525-549
25. Pestana JM. A unified constitutive model for clays and sands. *Ph.D. Thesis* MIT, Cambridge, Mass. 2000.
26. Praastrup, U. Three dimentional stress-strain behavior of soils tested in the danish rigid boundary true triaxial apparatus. *Ph.D. Thesis, Geotechnical engineering group, Aalborg University.* Aalborg University, 2000.
27. Roscoe KH, Schofield AN, Wroth CP. On yielding of soils *Géotechnique* 1958; **8**(1):22-53.
28. Schofield AN, Wroth CP. *Critical State Soil Mechanics* McGraw-Hill, London, 1968.
29. Simo JC, Ortiz M. A unified approach to finite deformation elastoplastic analysis based on the use of hyperelastic constitutive equations. *Computer Methods in Applied Mechanics and Engineering* 1985; **49**(2):221-245
30. Taiebat M, Shahir H, Pak A. Study of pore pressure variation during liquefaction using two constitutive models for sand. *Soil Dynamics and Earthquake Engineering* 2006; **27**(1):60-72
31. Wan RG, Guo, PJ. A simple constitutive model for granular soils: modified stress-dilatancy approach. *Computers and Geotechnics* 1998; **22**(2):109-133

32. Wood DM, Belkheir K, Liu DF. Strain softening and state parameters for sand modelling *Géotechnique* 1994; **44**(2):335-339
33. Wroth CP, Randolph MF, Houlsby GT, Fahey M. A review of the engineering properties of soils woth particular reference to the shear modulus. *Tech. Report CUED/D-SOILS TR75*, University of Cambridge, 1979
34. Wroth CP, Houlsby MF. Soil mechanics: property characterisation and analysis procedures. *Proc. 11th Int. Conf. Soil Mech. Found. Engng.*, San Francisco, May 1985, pp. 1-50